The Astrophysical Journal, 618:987–1000, 2005 January 10

APPARENT STELLAR WOBBLE BY A PLANET IN A CIRCUMSTELLAR DISK: LIMITATIONS ON PLANET DETECTION BY ASTROMETRY

Taku Takeuchi,[1,2] T. Velusamy,[3] and D. N. C. Lin[2]
Received 2004 June 1; accepted 2004 September 13

ABSTRACT

Astrometric detection of a stellar wobble on the plane of the sky will provide us the next breakthrough in searching for extrasolar planets. The *Space Interferometry Mission* (*SIM*) is expected to achieve high-precision astrometry as accurate as 1 μas, which is precise enough to discover a newborn Jupiter mass planet around a pre–main-sequence (PMS) star in the Taurus-Auriga star-forming region. PMS stars, however, have circumstellar disks that may be obstacles to the precise measurement of the stellar position. We present results on disk influences on the stellar wobble. The density waves excited by a planet move both the disk's mass center and the photocenter. The motion of the disk mass center induces an additional wobble of the stellar position, and the motion of the disk photocenter causes a contamination in the measurement of the stellar position. We show that the additional stellar motion dynamically caused by the disk's gravity is always negligible but that the contamination by the disk light can interfere with the precise measurement of the stellar position if the planet's mass is smaller than $\sim 10 M_{\rm J}$. The motion of the disk photocenter is sensitive to a slight change in the wave pattern and the disk properties. Measurements by interferometers are generally insensitive to extended sources such as disks. Because of this property, *SIM* will not suffer significant contamination by the disk light, even if the planet's mass is as small as $1 M_{\rm J}$.

Subject headings: accretion, accretion disks — astrometry — planetary systems: formation — solar system: formation

1. INTRODUCTION

Since the first discovery by Mayor & Queloz (1995), more than 120 extrasolar planets around main-sequence stars have been registered (Schneider 2004). Most of them were discovered by radial velocity measurement of stars (see, e.g., Marcy & Butler 1998; Perryman 2000). One of the planets that had already been found by the radial velocity measurement method has been confirmed to have transits on the star (Charbonneau et al. 2000), and a few planets were first discovered from their transits (Konacki et al. 2003a, 2003b). A gravitational microlensing event was reported to have been caused by a planet orbiting around binary stars (Bennett et al. 1999).

It is believed that astrometric detection of wobbling stars will be a strong method for discovering planets in the near future (McGrath et al. 2002; Benedict et al. 2002). A star orbiting the center of mass of the star-planet system draws an ellipse on the plane of the sky (after the parallax and the stellar proper motion are subtracted). The semimajor axis (in arcseconds) of the ellipse caused by a planet with a circular orbit is

$$a = \frac{M_p}{M + M_p} \frac{r_p/\mathrm{AU}}{d/\mathrm{pc}}, \tag{1}$$

where M_p and M are the masses of the planet and the star, respectively, r_p is the distance between the planet and the star, and d is the distance of the star from the observer. When a solar mass star with a Jupiter mass planet orbiting at 5 AU is observed from 10 pc, the amplitude of the stellar wobble is about 500 μas.

Measurement of stellar positions with a relative accuracy of sub-milliarcseconds is a challenge for ground-based optical observations. Recent improvement in interferometers has made it possible, and planet survey projects are ongoing at the Keck Interferometer and the Very Large Telescope Interferometer (for reviews, see Perryman 2000; Monnier 2003).

The *Space Interferometry Mission* (*SIM*), which is scheduled for launch in 2009, is expected to make significant progress in high-precision astrometry (Danner & Unwin 1999). *SIM* is expected to achieve ~ 1 μas relative accuracy with its narrow-angle astrometric mode. By the end of the 5 yr mission, it will be able to detect a Jupiter mass planet at 300 pc, or a Neptune mass planet at 20 pc, if it orbits at 1–5 AU around a $1 M_\odot$ star (Sozzetti et al. 2002). This high accuracy provides us an opportunity to search for newborn planets in star-forming regions. For example, the Taurus-Auriga molecular cloud, which is at 140 pc and has more than 200 T Tauri stars (Kenyon & Hartmann 1995), will be a good site for searching for a young planet. The discovery of a young planet around a pre–main-sequence (PMS) star will tell us when planet formation occurs. The standard scenario of planet formation assumes that planets form through coagulations of planetesimals (Hayashi et al. 1985; Lissauer 1993). According to an early version of this model (Pollack et al. 1996), it may take more than 10^7 yr to form a Jupiter mass planet at 5 AU. However, recent results on the oligarchic growth of planet cores (Kokubo & Ida 1998, 2000; Thommes et al. 2003) and reexamination of the effect of dust opacity in a protoplanet's envelope (Ikoma et al. 2000; Podolak 2003) indicate that the formation of a Jupiter mass planet may take much less time. In relatively massive disks where the asymptotic core masses are large, gas giant planets can also form rapidly and readily. However, in these disks, gravitational instability may also lead to the rapid formation of gas giants (Boss 1997). Although the formation timescale cannot be used to directly distinguish the paths of planet

[1] Earth and Planetary Sciences, Kobe University, Kobe 657-8501, Japan; taku@kobe-u.ac.jp.
[2] University of California Observatories/Lick Observatory, University of California, Santa Cruz, CA 95064; lin@ucolick.org.
[3] Jet Propulsion Laboratory, California Institute of Technology, MS 169-506, Pasadena, CA 91109.

formation, dynamical diversity may provide useful clues. In the gravitational instability scenario, planets are expected to form with large masses and eccentricities. In contrast, core accretion is expected to proceed in a tranquil environment with modest mass and low eccentricity. In the latter scenario, planets may acquire their dynamical diversity during disk evolution (Ida & Lin 2004) and depletion (Nagasawa et al. 2003). A systematic comparison between dynamical properties of protoplanets around PMS stars and those of mature planets around main-sequence stars provides a useful diagnostic on both the formation and evolution of planets and planetary systems. For example, Boss (1998) and Rice et al. (2003) calculated stellar wobbles induced by gravitationally unstable disks. Their models showed that disk fragmentation induces significantly larger or faster wobbles than in disks without fragmentation.

PMS stars, however, generally have circumstellar disks. The disk may be an obstacle to a planet search using astrometry. First, the planet disturbs the disk, as well as the star, and moves the position of the disk center off the star. The gravity of the disturbed disk induces an extra motion of the star, in addition to the direct wobbling by the planet. Second, the disturbance of the disk breaks the symmetry of the disk emission with regard to the star. The spiral waves excited by the planet make a wavy shape on the disk surface, leading to lighting and shadowing of the surface. The scattered light image of the disk is disturbed so as to have a spiral pattern, and the center of the disk light is moved away from the star. When the position of the star is measured by a small telescope (e.g., *SIM*'s telescopes are 33 cm in diameter), the beam size is much larger than the angular diameter of the disk; thus, the observable value is only the central position of the light from the star-disk system. If the shift of the photocenter of the system is similar to or larger than the amplitude of the dynamical stellar wobble, it is difficult to extract the dynamical motion from the apparent motion of the photocenter.

In order to examine how a circumstellar disk affects the precise measurement of the stellar position, we study the stellar wobble induced by a disk both dynamically (through its mass distribution) and illuminationally (through its scattered light distribution). In § 2, we calculate linear responses of the disk to the planet's gravity to obtain a spiral wave pattern. For simplicity, the disk is treated as two-dimensional and the planet's orbit as circular. In § 3, we examine the dynamical effect of the disk. The gravity exerted on the star by the disturbed disk is calculated, and the stellar wobble induced by the disk is compared with that by the planet. We show that the disk's dynamical effect can be neglected. In § 4, the motion of the central position of the disk light is calculated. We assume that the three-dimensional wavy pattern of the disk surface relates to the surface density fluctuation calculated in § 2, where the disk is treated as two-dimensional. The lighting and shadowing of the disk surface by starlight are calculated to make an image of the scattered light. The shift of the photocenter is calculated and compared with the dynamical motion of the star. In § 5, we apply our result to *SIM*. We simulate observations by *SIM* and calculate the anticipated astrometry shift induced by the disk light.

2. DENSITY WAVE EXCITATION BY A PLANET

2.1. *Wave Equations*

2.1.1. *Unperturbed Disk*

We consider a system composed of a central star, a circumstellar disk, and a planet in the disk. The planet's orbit is assumed to be circular with an angular velocity

$$\Omega_p = \left(\frac{GM}{r_p^3}\right)^{1/2}, \tag{2}$$

where we ignore contributions from the planet's mass M_p and the disk mass M_d, assuming $M_p, M_d \ll M$.

A planet embedded in a gas disk opens a gap around its orbit, provided that the planet's mass is larger than Neptune or Saturn's mass [$(1-3)\times 10^{-4}\ M_\odot$; Takeuchi et al. 1996]. The gap width is in general a function of the planet's mass, the gas sound speed, and the gas viscosity. For a low-mass planet like Neptune, the gap width is of the order of the disk thickness, while for a Jupiter mass planet, the gap spreads from the $m = 2$ inner Lindblad resonance (at $0.63r_p$) to the $m = 2$ outer Lindblad resonance (at $1.31r_p$; Lin & Papaloizou 1986; Takeuchi et al. 1996). In this work, we consider an unperturbed surface density distribution of a disk with a gap, and for simplicity, it is written

$$\sigma_0 = f_{\rm gap}\sigma_* r_{\rm AU}^{-1}, \tag{3}$$

where $r_{\rm AU}$ is the nondimensional radial coordinate normalized by 1 AU and σ_* is the surface density at 1 AU. We assume that the surface density decreases with r as a power law with an index of 1, and near the planet's orbit it drops; $f_{\rm gap}$ is unity except for in the planet's neighborhood, where it drops to zero. We use an approximate expression for the gap shape:

$$f_{\rm gap} = \frac{\exp(\pm 2x)}{\exp(\pm 2x) + 1}, \tag{4}$$

where the upper and lower signs are for the disk outside the planet's orbit and for the inner disk, respectively, and the nondimensional distance x from the gap edge is

$$x = \frac{r - r_{g,\,\rm out}}{\Delta_{\rm edge}} \tag{5}$$

for the outer disk and

$$x = \frac{r - r_{g,\,\rm in}}{\Delta_{\rm edge}} \tag{6}$$

for the inner disk. The median locations of the gap edges, $r_{g,\,\rm out}$ and $r_{g,\,\rm in}$, are expediently defined as the points where the surface density drops to half the value of the no-gap disk. The edge width $\Delta_{\rm edge}$ is of order of the disk half-thickness h. The half-width of the gap is $\Delta_g = (r_{g,\,\rm out} - r_{g,\,\rm in})/2$. We assume that the gap shape is symmetrical with regard to the planet's position and that $\Delta_g = r_{g,\,\rm out} - r_p = r_p - r_{g,\,\rm in}$.

A polytropic equation of state with an index γ is assumed for the gas. The two-dimensional pressure is $P_0 = K\sigma_0^\gamma$. The enthalpy and the sound speed are expressed by

$$\eta_0 = \frac{\gamma}{\gamma - 1} K\sigma_0^{\gamma-1}, \tag{7}$$

$$c_0^2 = (\gamma - 1)\eta_0, \tag{8}$$

respectively. The gas rotation law is assumed to be Keplerian: $\Omega^2 = GM/r^3$. Although in actual disks the gas pressure makes

the rotation slightly slower than Keplerian, we neglect this small difference. For a given enthalpy distribution, the half-thickness of the unperturbed disk is $h = (2\eta_0)^{1/2}/\Omega$. The derivation of this equation is discussed in § 4.1.1.

2.1.2. *Perturbation by a Planet*

We solve the gas motions perturbed by the planet's gravity. The gap around the planet's orbit divides the disk into two parts. The perturbation equations are solved separately for the inner and outer disks. We use cylindrical coordinates (r, θ). For the inner disk the coordinate origin is set on the central star, and the coordinates are not an inertial frame. On the other hand, for the outer disk the origin is on the center of mass of the system. We neglect the self-gravity of the disk.

The planet's perturbation potential on the inner disk is written as

$$\phi_1 = -\frac{GM_p}{\left[r_p^2 + r^2 - 2r_p r\cos(\theta - \Omega_p t)\right]^{1/2}} + \frac{GM_p r\cos(\theta - \Omega_p t)}{r_p^2}. \quad (9)$$

The second term is the indirect term that represents the inertial force. For the outer disk, the star also orbits the origin and causes a perturbation. The perturbation potential is

$$\phi_1 = -\frac{GM}{[r_a^2 + r^2 - 2r_a r\cos(\theta - \Omega_p t - \pi)]^{1/2}} - \frac{GM_p}{[r_b^2 + r^2 - 2r_b r\cos(\theta - \Omega_p t)]^{1/2}}, \quad (10)$$

where $r_a = r_p M_p/(M + M_p)$ and $r_b = r_p M/(M + M_p)$ are the distances from the origin to the star and to the planet, respectively.

We solve for Fourier components of the perturbations. Each perturbation variable, which is with subscript "1," is decomposed in the azimuthal direction as

$$X_1(r,\theta) = \sum_{m=0}^{\infty} \mathrm{Re}\{X_{1,m}(r)\exp[im(\theta - \Omega_p t)]\}, \quad (11)$$

where m is the wavenumber in the θ-direction. In the following part of the paper, we solve Fourier components $X_{1,m}$, but we omit subscript "m" in writing whenever this omission does not cause any confusion.

The perturbation equations are (Goldreich & Tremaine 1979)

$$im(\Omega - \Omega_p)u_1 - 2\Omega v_1 = -\frac{d}{dr}(\phi_1 + \eta_1), \quad (12)$$

$$im(\Omega - \Omega_p)v_1 + 2Bu_1 = -\frac{im}{r}(\phi_1 + \eta_1), \quad (13)$$

$$im(\Omega - \Omega_p)\sigma_1 + \frac{1}{r}\frac{d}{dr}(r\sigma_0 u_1) + \frac{im\sigma_0}{r}v_1 = 0, \quad (14)$$

where u_1 and v_1 are, respectively, the radial and azimuthal components of the velocity perturbation and Oort's $B = \Omega + (r/2)(d\Omega/dr)$. The enthalpy perturbation relates to σ_1 as

$$\eta_1 = c_0^2\frac{\sigma_1}{\sigma_0}. \quad (15)$$

The Fourier transformed perturbation potential ϕ_1 for the inner disk is expressed as

$$\phi_1(r) = -\frac{GM_p(2 - \delta_{m0})}{2r_p}b_{1/2}^m(\beta) + \frac{GM_p r}{r_p^2}\delta_{m1}, \quad (16)$$

where $\beta = r/r_p$, δ_{mn} is Kronecker's δ, and $b_{1/2}^m$ is the Laplace coefficient,

$$b_{1/2}^m(\beta) = \frac{2}{\pi}\int_0^{\pi}\frac{\cos m\phi\, d\phi}{(1 - 2\beta\cos\phi + \beta^2)^{1/2}}. \quad (17)$$

For the outer disk,

$$\phi_1(r) = (-1)^{m-1}\frac{GM(2 - \delta_{m0})}{2r_a}b_{1/2}^m(\beta_a) - \frac{GM_p(2 - \delta_{m0})}{2r_b}b_{1/2}^m(\beta_b), \quad (18)$$

where $\beta_a = r/r_a$ and $\beta_b = r/r_b$.

2.2. *Numerical Integration*

We expect that the planet excites steady waves in the disk; i.e., in the frame rotating with the planet, the wave pattern keeps the same shape. In such a steady state, energy input to the waves from the planet is balanced by the energy loss of wave dissipation caused by shocks or viscous damping. This situation is numerically expressed by allowing the waves to freely escape from the boundaries of the computational domain; i.e., we take the radiative boundary condition.

We solve the perturbation equations of the inner and outer disks separately. In solving the inner disk, the numerical integration starts from the point $r_{\mathrm{in},2}$ near the planet, at which the gas density is sufficiently low. Equations (12)–(14) are solved inward to a certain radius $r_{\mathrm{in},1}$, where the waves wind tightly enough. For the outer disk, the computation is performed for $[r_{\mathrm{out},1}, r_{\mathrm{out},2}]$.

The computational boundaries of the planet's side are at the gap edges, $r_{\mathrm{in},2} = r_{g,\mathrm{in}} + 2\Delta_{\mathrm{edge}}$ for the inner disk and $r_{\mathrm{out},1} = r_{g,\mathrm{out}} - 2\Delta_{\mathrm{edge}}$ for the outer disk. The densities at these boundaries are about 2% of the nongap values (eq. [4]). We adopt the free boundary condition. The Lagrange derivative of the enthalpy is zero: $D\eta/Dt = 0$. Assuming that the radial derivative of the unperturbed enthalpy is zero, we simply have $\eta_1 = 0$.

Equations (12)–(14) are integrated using the fourth-order Runge-Kutta method. The Laplace coefficients (17) are numerically calculated using the method by Korycansky & Pollack (1993). The boundary condition at $r_{\mathrm{in},1}$ or $r_{\mathrm{out},2}$ is radiative. At these points, only an outgoing wave is allowed to exist. In a WKB approximation, the enthalpy perturbation is expressed as $\eta_1 = H(r)\exp[\int ik\, dr]$, where $k = \pm\sqrt{-D}/c_0$ and $D = \Omega^2 - m^2(\Omega - \Omega_p)^2$ (eq. [19] in Goldreich & Tremaine 1979 with $G = 0$, $\omega = m\Omega_p$, and $\kappa = \Omega$). The radiative boundary condition is, as in Korycansky & Pollack (1993),

$$\frac{d\eta_1}{dr} = \left(\frac{1}{H}\frac{dH}{dr} + ik\right)\eta_1, \quad (19)$$

where we take a positive sign of the wavenumber k (the negative sign corresponds to the incoming wave). The derivative of the amplitude of η_1 is calculated in a similar way by

deriving equation (18b) in Goldreich & Tremaine (1979) and is

$$\frac{1}{H}\frac{dH}{dr} = -\frac{1}{2}\frac{d}{dr}\ln\left(\frac{r\sigma_0 k}{D}\right). \tag{20}$$

For the $m = 1$ mode in the inner disk, there is no wave zone (i.e., k is purely imaginary). We use the free boundary condition ($\eta_1 = 0$) at both $r_{\mathrm{in},1}$ and $r_{\mathrm{in},2}$.

2.3. *Viscous Damping of Waves*

The calculations in the previous subsections do not take any wave damping into account. In actual disks, waves attenuate through viscous dissipation or shock dissipation. Here we consider viscous wave damping, which works even though the wave amplitude is not large enough to cause shocks. Waves are excited near the planet and propagate away. As they propagate farther, their amplitudes decline through the viscous dissipation. We write the enthalpy perturbation in a viscous disk as

$$\eta_{1,\mathrm{vis}} = f_{\mathrm{vis}}\eta_1, \tag{21}$$

where η_1 is the enthalpy solved for the nonviscous disk in the previous subsection and f_{vis}, a factor of viscous damping, is unity near the planet and goes to zero with the distance from the planet. From equations (A10) and (A15) in Takeuchi et al. (1996), the damping factor is written as

$$f_{\mathrm{vis}} = \exp\left(-\int_{r_{\mathrm{L},m}}^{r}\left\{\zeta + \left[\frac{4}{3} + \frac{\Omega^2}{m^2(\Omega-\Omega_p)^2}\right]\nu\right\} \times \frac{m(\Omega_p-\Omega)}{2c_0^2}k\,d\tilde{r}\right), \tag{22}$$

where $r_{\mathrm{L},m}$ is the radius of the Lindblad resonance of the mth mode wave and ζ and ν are the bulk and shear viscosities, respectively. For simplicity, we use the α prescription for viscosity: $\zeta = \nu = \alpha_{\mathrm{vis}}c_0^2/\Omega$. The radial wavenumber is $k = \sqrt{-D}/c_0$ for outgoing waves.

2.4. *Wave Properties*

In this subsection, we present properties of the density waves excited by a planet. The wave patterns are different from the ones derived by Korycansky & Pollack (1993) because of the assumptions that the disk has a gap and that the waves viscously dissipate.

As a fiducial model, we adopt the following parameters: The central star's mass is $M = 1\ M_\odot$. The planet's orbital radius is $r_p = 5$ AU. The surface density profile is $\sigma_0 = 1000 f_{\mathrm{gap}} r_{\mathrm{AU}}^{-1}$ g cm^{-3} with a gap of the half-width $\Delta_g = 0.4r_p$ and the edge width $\Delta_{\mathrm{edge}} = 5\times10^{-2}r_p$. The disk inner radius is $r_{\mathrm{in},1} = 0.01r_p$, and the outer radius is $r_{\mathrm{out},2} = 5r_p$. The polytrope index is $\gamma = 1.4$. The sound speed at 1 AU is $c_0(1\ \mathrm{AU}) = 10^5$ cm s^{-1}. The viscosity parameter is $\alpha_{\mathrm{vis}} = 10^{-2}$. The planet's mass is arbitrary in linear calculations. We take a Jupiter mass planet ($M_p = 10^{-3}\ M_\odot$) as a typical value in the following discussions.

Figure 1 shows which modes are effectively excited. The angular momentum flux of waves is a convenient value to compare, and its expression is written by Goldreich & Tremaine (1979) as

$$F_A = \frac{\pi m r \sigma_0}{\Omega^2 - m^2(\Omega-\Omega_p)^2} \times\left[\mathrm{Im}\,(\eta_1)\mathrm{Re}\,\frac{d}{dr}(\phi_1+\eta_1) - \mathrm{Re}\,(\phi_1+\eta_1)\mathrm{Im}\,\frac{d\eta_1}{dr}\right], \tag{23}$$

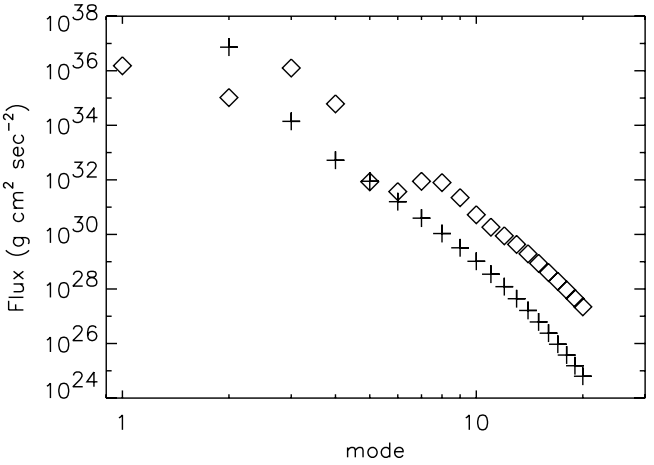

FIG. 1.—Angular momentum fluxes carried by the waves of various modes m. The diamonds and plus signs show fluxes in the outer disk and in the inner disk, respectively.

where Re and Im mean the real and imaginary parts, respectively. Fluxes F_A are evaluated for waves without viscous damping. For such waves, F_A converges to a certain value at locations far enough from the planet (see Fig. 7 in Korycansky & Pollack 1993). In Figure 1, converged values of F_A are plotted. Except for small fluctuations, the angular momentum flux is a decreasing function of mode m, and waves of $m \lesssim 3$ dominate. High $m \gtrsim 3$ waves are not excited strongly because their Lindblad resonances (LRs) are buried in the gap (Artymowicz & Lubow 1994). The locations of LRs are closer to the planet for higher m (for a schematic illustration, see Fig. 1 in Takeuchi et al. 1996). The resonance positions of the $m = 3$ wave are $r_{\mathrm{L},3} = 0.76r_p$ and $1.21r_p$, which are inside the gap of half-width $\Delta_g = 0.4r_p$, while $m = 2$ LRs at $0.63r_p$ and at $1.31r_p$ are marginally on the gap edges.

Waves cannot freely travel through the disk. If the disk viscosity is large enough, waves attenuate before they reach the disk inner or outer boundaries. Figure 2 shows the damping factors, f_{vis}, for various m of waves. Higher m waves dissipate more quickly, and lower m waves can travel farther away from the planet. If the disk viscosity is large ($\alpha_{\mathrm{vis}} = 10^{-2}$), however, even an $m = 2$ wave cannot reach the central star nor the outer part farther than $4r_p$. An $m = 2$ wave can reach the central star if the viscosity is as small as $\alpha_{\mathrm{vis}} = 10^{-3}$, although it cannot travel farther than $8r_p$. Even in such a low-viscosity disk, $m \gtrsim 5$ waves dissipate before they reach the central star.

The above results are summarized as follows. After the opening of a gap by a planet, the excitation of high m waves is suppressed. Only $m \lesssim 3$ waves can be excited. These waves may propagate close to the central star, although they dissipate before arriving at $\sim 4r_p$ in a viscous disk of $\alpha_{\mathrm{vis}} = 10^{-2}$. The wave propagation changes the disk shape inside $\sim 4r_p$. Figure 3 shows the surface density perturbation. The perturbations of $m = 1-20$ are summed up to construct the wave pattern. In the inner disk, however, the $m = 2$ wave dominates the wave pattern, while in the outer disk the $m = 1$ wave dominates. This is because there is no inner LR for $m = 1$ and because $m \gtrsim 3$ LRs are buried in the gap. The wave amplitude declines under the viscous damping at larger distances from the planet.

3. DYNAMICAL STELLAR WOBBLE

A planet wobbles its central star. While the planet's gravity shifts the stellar position directly, if there is a circumstellar

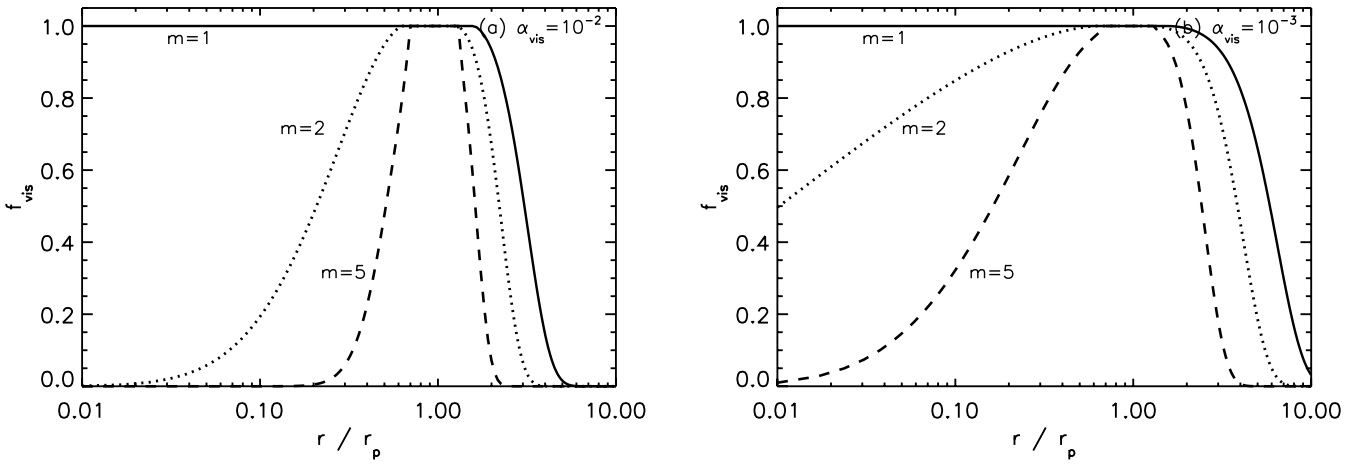

FIG. 2.—Wave damping factor $f_{\rm vis}$. The solid, dotted, and dashed lines correspond to $m = 1$, 2, and 5 waves, respectively. The damping factor (eq. [22]) is calculated for the inner part inside the inner Lindblad resonances (ILRs) and for the outer part outside the outer Lindblad resonances (OLRs). Between the ILR and the OLR, $f_{\rm vis}$ is assumed to be unity. For the $m = 1$ wave, there is no ILR and $f_{\rm vis}$ is set to unity in the inner disk inside the planet's orbit. (*a*) $\alpha_{\rm vis} = 10^{-2}$. (*b*) $\alpha_{\rm vis} = 10^{-3}$.

disk, the planet affects the stellar position through altering the disk density distribution as well. Since the $m = 1$ wave pattern does not have any symmetry that conserves the center of mass of the disk, the disk's mean position moves. Because the mass center of a system composed of a star, a planet, and a disk must be conserved, the star moves so as to compensate for the motions of the planet and the disk.

The disk's gravitational attraction to the star is considered in this section, although the disk self-gravity is ignored in the calculation of wave excitation. This treatment is justified if the perturbation of the disk's gravitational potential is much smaller than the gas enthalpy perturbation. When the Toomre Q value, which is $c_0\Omega/(\pi G\sigma_0)$, is much larger than 1, this condition is satisfied (see also the discussion by Ward 1986). In our model, $Q = 19$ at 10 AU.

In the previous sections, different coordinate systems have been used for the inner and outer disks. We use hereafter the coordinates (r, θ, z) and the corresponding Cartesian coordinates (x, y, z), whose origin is set to the star. When we need to refer to coordinates whose origin is on the center of mass, the coordinate variables are distinguished by writing (r', θ', z).

The x-position of the center of mass of the inner disk is given by

$$x_{d,\rm in} = \frac{1}{M_{d,\rm in}} \int_{r_{\rm in,1}}^{r_{\rm in,2}} \int_0^{2\pi} \sum_m \mathrm{Re}\,\{\sigma_{1,m}(r) \times \exp\,[im(\theta - \Omega_p t)]\} r^2 \cos\theta\, d\theta\, dr$$
$$= \frac{\pi}{M_{d,\rm in}} \int_{r_{\rm in,1}}^{r_{\rm in,2}} r^2 [\mathrm{Re}\,(\sigma_{1,1}) \cos\,(\Omega_p t) + \mathrm{Im}\,(\sigma_{1,1}) \sin\,(\Omega_p t)]\, dr, \quad (24)$$

where $M_{d,\rm in}$ is the inner disk mass and the subscript "m" is written explicitly. Because of the symmetry, all the contributions vanish after θ-integration except for the $m = 1$ mode. For the outer disk the disk variables are calculated in the inertial frame, and then

$$x_{d,\rm out} = \frac{\pi}{M_{d,\rm out}} \int_{r'_{\rm out,1}}^{r'_{\rm out,2}} r'^2 [\mathrm{Re}\,(\sigma_{1,1}) \cos\,(\Omega_p t) + \mathrm{Im}\,(\sigma_{1,1}) \sin\,(\Omega_p t)]\, dr' + r_a \cos\,(\Omega_p t), \quad (25)$$

where the second term represents the motion of the inertial coordinates (r', θ', z) to the star. The y-positions of the centers of mass are similarly

$$y_{d,\rm in} = \frac{\pi}{M_{d,\rm in}} \int_{r_{\rm in,1}}^{r_{\rm in,2}} r^2 [\mathrm{Re}\,(\sigma_{1,1}) \sin\,(\Omega_p t) - \mathrm{Im}\,(\sigma_{1,1}) \cos\,(\Omega_p t)]\, dr, \quad (26)$$

$$y_{d,\rm out} = \frac{\pi}{M_{d,\rm out}} \int_{r'_{\rm out,1}}^{r'_{\rm out,2}} r'^2 [\mathrm{Re}\,(\sigma_{1,1}) \sin\,(\Omega_p t) - \mathrm{Im}\,(\sigma_{1,1}) \cos\,(\Omega_p t)]\, dr' + r_a \sin\,(\Omega_p t). \quad (27)$$

The coordinates' origin is set to the star, and the planet's position is $(x_p, y_p) = [r_p \cos\,(\Omega_p t),\ r_p \sin\,(\Omega_p t)]$. The center of

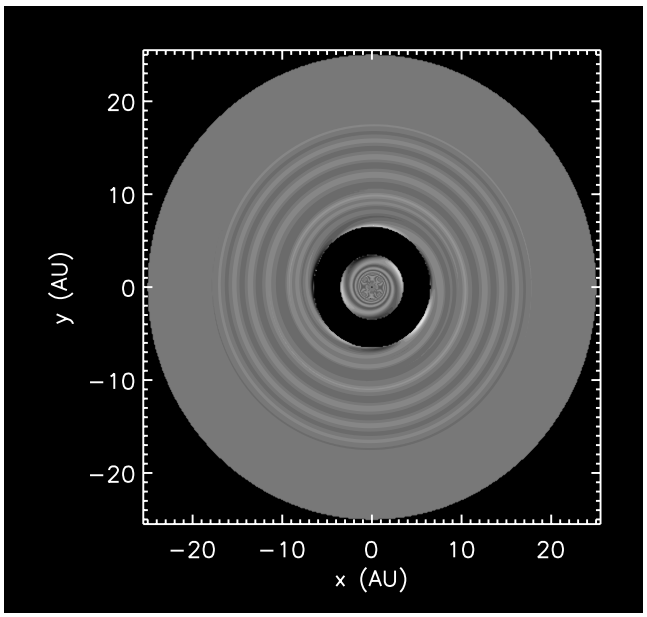

FIG. 3.—Surface density perturbation normalized by the unperturbed value, $\sigma_1(r)/\sigma_0(r)$. A planet is at (5, 0) and opens a gap.

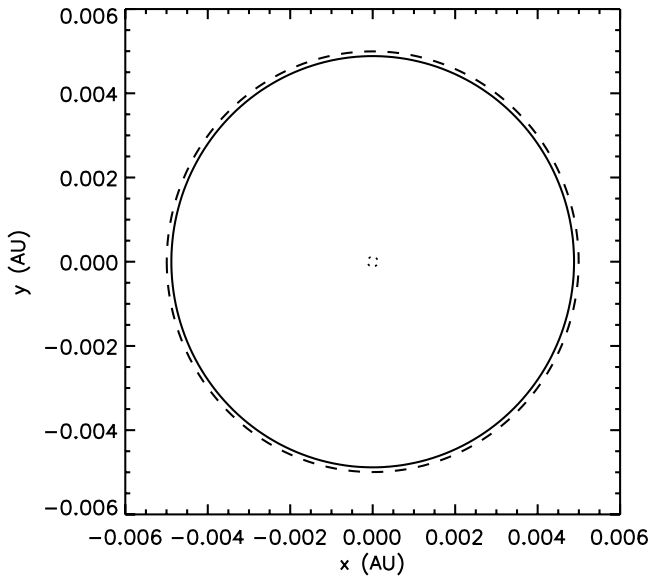

FIG. 4.—Movement of the stellar position in the inertial coordinates. A Jupiter mass planet orbits at 5 AU. The movement caused by both the planet and the disk is shown by the solid line. The dashed line shows the movement caused only by the planet, ignoring the disk's effect. The dotted line shows the contribution of the disk (the difference between the solid and dashed lines).

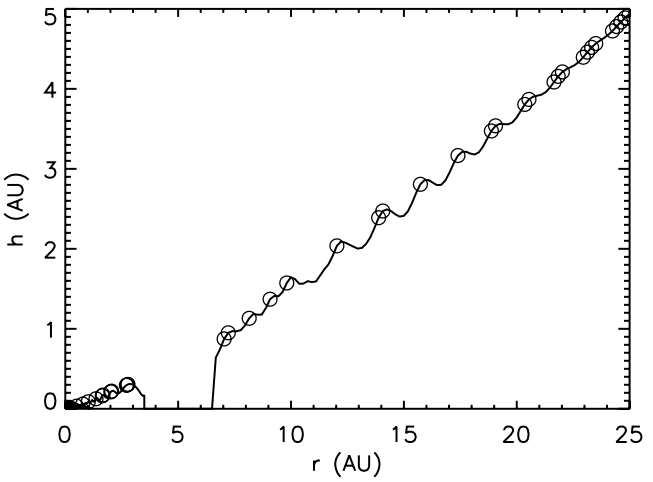

FIG. 5.—Fluctuation of the disk surface. A variation in the disk half-thickness in the planet's direction ($\theta = \Omega_p t$) is shown by the solid line. The portions marked by the circles are directly illuminated by the star. To show the fluctuation clearly, we use a model with a $10M_J$ planet ($M_p = 10M_J$) at 5 AU. A gap opens around the planet's orbit.

mass of the entire system, which does not move in an inertial coordinate system, is

$$x_{\rm CM} = \frac{M_p x_p + M_{d,\rm in} x_{d,\rm in} + M_{d,\rm out} x_{d,\rm out}}{M_s + M_p + M_{d,\rm in} + M_{d,\rm out}}, \quad (28)$$

$$y_{\rm CM} = \frac{M_p y_p + M_{d,\rm in} y_{d,\rm in} + M_{d,\rm out} y_{d,\rm out}}{M_s + M_p + M_{d,\rm in} + M_{d,\rm out}}. \quad (29)$$

The disk contribution to the stellar wobble is negligibly small compared to the planet's direct effect. Only the $m = 1$ perturbation shifts the center of mass of the disk, and the amplitude of the $m = 1$ wave is not large enough to make a significant movement. There is no $m = 1$ LR in the inner disk, and no significant $m = 1$ wave is excited there. For the outer disk the $m = 1$ wave is excited at the outer LR ($r_{\rm L,1} = 1.59 r_p$), which, however, is not very close to the planet, and only a relatively weak wave is excited. Although the wave amplitude is proportional to the planet's mass, the amplitude of stellar wobble by the planet itself is also proportional to the mass. Thus, the relative importance of the disk to the planet does not change for different planets' masses.

Figure 4 shows the motion of the star. The motion induced both by the planet and by the disk (*solid line*) does not differ significantly from the motion induced only by the planet (*dashed line*). In this figure, we assumed that the disk mass is 10 times the typical model. The disk mass inside 25 AU is 0.16 $M_\odot$, which is probably close to the upper limit of real disks. Even such a massive disk makes a minor contribution to the stellar wobble. Because the disk contribution is proportional to the disk mass, it is negligible for most actual disks.

4. WOBBLE OF THE PHOTOCENTER

Although a disk does not perturb the stellar position significantly, its presence may obstruct the precise measurement of the stellar position. In a realistic observation, the position of a star is measured using a relatively large beam that covers the entire star-disk system. The mean location of the light from both the star and the disk is interpreted as the position of the former. If the disk is distorted and its light has any asymmetry, it may shift the apparent position of the star. In this section, we calculate the motion of the photocenter. The photocenter is the mean location of a star-disk system that is weighted by its surface brightness. In our problem, the central star and the disk contribute to the photocenter, while the planet's radiation is neglected. A Jupiter mass planet is $10^{-5}\ L_\odot$ at the age of 10^6 yr and $3\times10^{-6}\ L_\odot$ at 10^7 yr, and a $10M_J$ planet is $\sim10^{-3}\ L_\odot$ at the age of 10^6–10^7 yr (Burrows et al. 1997). The ratio of the luminosities of the planet and the star, L_p/L, is much smaller than their mass ratio, M_p/M. When a circumplanetary disk forms, its emission may contribute (Lubow et al. 1999; Tanigawa & Watanabe 2002; Bate et al. 2003; D'Angelo et al. 2003). We neglect the circumplanetary disk's contribution, assuming that most of the disk material has accreted to the planet.

4.1. *Scattered Light from the Disk*

In our calculations of the disk radiation, we make the following assumptions for simplicity. We consider optical light images of the disks. At the optical wavelengths, the disk radiation is dominated by the scattered light of the central star, and the disk thermal emission is neglected. In addition, the disk is treated as completely opaque. Incident starlight cannot penetrate the disk surface, but is completely scattered (i.e., the albedo is unity). Thus, when the disk surface waves, only the regions that face the star directly shine, making the disk striped. Figure 5 shows a section of a disk in the *r*-*z* plane. The surface parts that are illuminated by the star are indicated by circles. The other parts are assumed to be totally dark so they do not scatter any light. These assumptions make the model disks have more contrasts than actual disks. In real disks, starlight can penetrate somewhat inside the surface, and the stripes do not have clear boundaries between the light and dark parts, making the contrast lower. In addition, the assumption that the incident starlight is totally scattered at the disk surface without any absorption also works to overestimate the disk's contrast. Hence, the motions of the photocenters of model disks are more sensitive to the perturbations than actual ones. The calculations

below should be considered to give an upper limit of the photocenter shift.

4.1.1. *Variation in the Disk Thickness*

Fluctuation of the disk surface is calculated from the results of the wave pattern in the previous sections. We assume that the disk always keeps hydrostatic equilibrium in the vertical direction. For the inner disk,

$$-\frac{GMz}{(r^2+z^2)^{3/2}} - \frac{GM_p z}{\left[r^2+r_p^2-2rr_p\cos(\theta-\Omega_p t)+z^2\right]^{3/2}} - \frac{1}{\rho}\frac{dp}{dz} = 0, \quad (30)$$

where ρ is the gas density and p is the three-dimensional gas pressure. We assume $z \ll r$. In addition, outside the Roche lobe $[|r-r_p| \gg (M_p/M)^{1/3} r_p]$, the gravity of the planet (the second term) is negligible compared to the gravity of the star (the first term). In our model disks, the opening gap clears out the gas around the planet's orbit, and there remains little gas inside the Roche lobe (we ignore the circumplanetary disk). The above equation reduces to

$$-\frac{GMz}{r^3} - \frac{1}{\rho}\frac{dp}{dz} = 0. \quad (31)$$

We use the adiabatic equation of state, $p = K_3\rho^{\gamma_3}$. Then, we have the density profile in the z-direction

$$\rho = \rho_{\rm mid}\left[1-\left(\frac{z}{h}\right)^2\right]^{1/(\gamma_3-1)}, \quad (32)$$

where the subscript "mid" means the value at the disk midplane, and the disk half-thickness is

$$h(r,\theta) = \frac{1}{\Omega(r)}\sqrt{\frac{2\gamma_3}{\gamma_3-1}\frac{p_{\rm mid}(r,\theta)}{\rho_{\rm mid}(r,\theta)}} = \frac{1}{\Omega(r)}\sqrt{2\eta_{\rm mid}(r,\theta)}. \quad (33)$$

This equation relates the disk half-thickness to the midplane density and the pressure, although in the previous sections we calculated only the two-dimensional values of the density and the pressure. It is shown in Appendix A that a similar relation,

$$h(r,\theta) = \frac{1}{\Omega(r)}\sqrt{\frac{2\gamma}{\gamma-1}\frac{P(r,\theta)}{\sigma(r,\theta)}} = \frac{1}{\Omega(r)}\sqrt{2\eta(r,\theta)}, \quad (34)$$

holds for the two-dimensional values.

The variables of the outer disk are defined on the inertial coordinates (r', θ', z). The hydrostatic equilibrium is expressed as

$$-\frac{GMz}{\left[r'^2+r_a^2-2r'r_a\cos(\theta-\Omega_p t-\pi)+z^2\right]^{3/2}} - \frac{GM_p z}{\left[r'^2+r_b^2-2rr_b\cos(\theta-\Omega_p t)+z^2\right]^{3/2}} - \frac{1}{\rho}\frac{dp}{dz} = 0. \quad (35)$$

For the outer disk, $r' \gg r_a$. We assume $r' \gg z$; then, outside the Roche lobe $[|r'-r_b| \gg (M_p/M)^{1/3} r_b]$, the above equation reduces to

$$-\frac{GMz}{r'^3} - \frac{1}{\rho}\frac{dp}{dz} = 0. \quad (36)$$

Then, we have an expression of h similar to that for the inner disk,

$$h(r',\theta') = \frac{1}{\Omega(r')}\sqrt{\frac{2\gamma}{\gamma-1}\frac{P(r',\theta')}{\sigma(r',\theta')}} = \frac{1}{\Omega(r')}\sqrt{2\eta(r',\theta')}, \quad (37)$$

where $\Omega^2(r') = GM/r'^3$.

A disk height variation induced by a $10M_{\rm J}$ planet is shown in Figure 5. We assume that the disk has an opaque surface at h, and starlight is totally scattered at the surface. Only the parts that are illuminated directly by the star emit radiation, while the other parts are totally dark.

4.1.2. *Scattered Light Flux from the Disk*

We neglect the star's diameter. The starlight emerges from the origin. If there is no obstacle on the ray to a part of the disk surface, that part is illuminated by the star. The parts marked by circles in Figure 5 are illuminated. The starlight is assumed to be totally scattered at the disk surface (r, θ, h). Although the actual scattering occurs at the photosurface of constant optical depth, which is below the disk surface, we approximate the photosurface by the disk surface. In Appendix B, this approximation is examined. Consider an illuminated part at (r, θ, h) on the inner disk. An area $rdrd\theta$ on the x-y plane (midplane) corresponds to an area of the disk surface $dS = rdrd\theta/\cos\varphi$, where φ is an angle between the normal vector $\boldsymbol{n}$ of the surface and the z-axis. The surface dS receives a stellar energy flux

$$dL_d = L\frac{\cos\alpha\, dS}{4\pi r^2}, \quad (38)$$

where L is the stellar luminosity and α is the angle between the normal vector $\boldsymbol{n}$ and the line from dS to the star. To derive $\cos\alpha$, we assume that the waves wind so tightly that $dh/d\theta$ is neglected in comparison with dh/dr; i.e., the toroidal component of the normal vector $\boldsymbol{n}$ is neglected and $\boldsymbol{n} = (n_r, n_\theta, n_z) \approx (-\sin\varphi, 0, \cos\varphi)$. We then have

$$\cos\alpha = \sin\beta\sin\varphi - \cos\beta\cos\varphi, \quad (39)$$

where β is the angle between the ray of starlight to dS and the z-axis. For simplicity, we assume that the scattering at the disk surface is isotropic. The intensity of the scattered light is

$$I = \frac{dL_d}{\pi dS} = \frac{L\cos\alpha}{4\pi^2 r^2}. \quad (40)$$

An observer looks at the disk with a viewing angle v ($v = 0$ at face-on), using a detector that has a solid angle $d\Omega$ from the disk. We define the angle δ between the line of sight (pointing to the observer) and the normal vector $\boldsymbol{n}$, which satisfies

$$\cos\delta = -\sin v\sin\varphi\cos\theta + \cos v\cos\varphi. \quad (41)$$

The scattered light flux from the surface element dS to the detector is then

$$dF_d = I\cos\delta\, dS\, d\Omega \approx \frac{L}{4\pi^2 r^2}\left[1+\left(\frac{dh}{dr}\right)^2\right]^{-1/2}\left(\frac{dh}{dr}-\frac{h}{r}\right) \times\left(\cos v-\frac{dh}{dr}\sin v\cos\theta\right) r\,dr\,d\theta\,d\Omega, \quad (42)$$

where we used

$$\sin\beta=\frac{r}{(r^2+h^2)^{1/2}}\approx 1,\quad \cos\beta=\frac{h}{(r^2+h^2)^{1/2}}\approx\frac{h}{r}, \quad (43)$$

$$\sin\varphi=\frac{dh}{dr}\left[1+\left(\frac{dh}{dr}\right)^2\right]^{-1/2},\quad \cos\varphi=\left[1+\left(\frac{dh}{dr}\right)^2\right]^{-1/2}, \quad (44)$$

and $h \ll r$.

Next, consider an illuminated part at (r', θ', h) on the outer disk. The disk surface $dS' = r'dr'd\theta'/\cos\varphi'$ receives a stellar energy flux

$$dL_d = L\frac{\cos\alpha' dS'}{4\pi r^2}, \quad (45)$$

where r is the distance between the disk surface element dS' and the star and

$$\cos\alpha' = \sin\beta\sin\varphi' - \cos\beta\cos\varphi' + O\left(\frac{r_a}{r}\right)^2, \quad (46)$$

$$\sin\beta=\frac{r}{(r^2+h^2)^{1/2}}\approx 1,\quad \cos\beta=\frac{h}{(r^2+h^2)^{1/2}}\approx\frac{h}{r}, \quad (47)$$

$$\sin\varphi'=\frac{dh}{dr'}\left[1+\left(\frac{dh}{dr'}\right)^2\right]^{-1/2},\quad \cos\varphi'=\left[1+\left(\frac{dh}{dr'}\right)^2\right]^{-1/2}. \quad (48)$$

The intensity of the scattered light from dS' is

$$I=\frac{dL_d}{\pi dS'}=\frac{L\cos\alpha'}{4\pi^2 r^2}. \quad (49)$$

The scattered light flux is

$$dF_d = I\cos\delta'\, dS'\, d\Omega \approx \frac{L}{4\pi^2 r^2}\left[1+\left(\frac{dh}{dr'}\right)^2\right]^{-1/2}\left(\frac{dh}{dr'}-\frac{h}{r}\right) \times\left(\cos v-\frac{dh}{dr'}\sin v\cos\theta'\right) r'dr'\,d\theta'\,d\Omega, \quad (50)$$

where

$$\cos\delta' = -\sin v\sin\varphi'\cos\theta' + \cos v\cos\varphi'. \quad (51)$$

A simulated image of a face-on disk is shown in Figure 6.

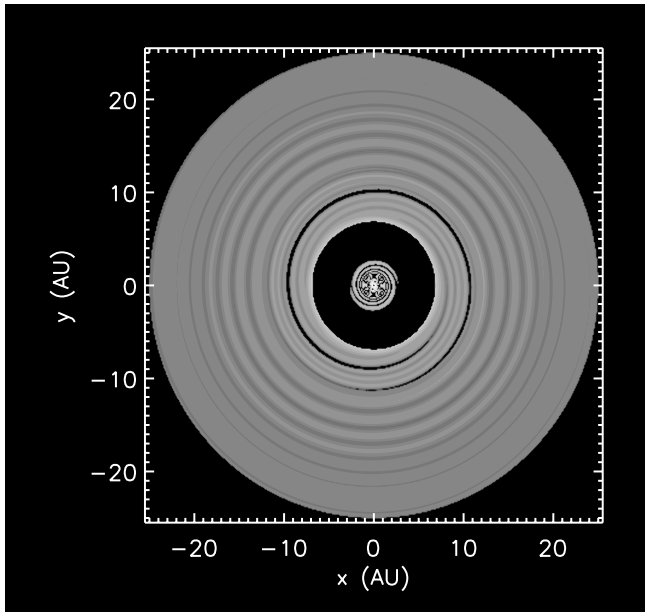

FIG. 6.—Simulated scattered light image of a face-on disk. The disk is perturbed by a Jupiter mass planet ($M_p = M_J$). Gray scale shows logarithmic values of the disk flux.

4.2. *Motion of the Photocenter*

4.2.1. *Face-on Disks*

If a disk is observed at face-on ($v = 0$), then the most important mode in moving the photocenter is the $m = 1$ wave, which also shifts the mass center of the disk. Modes of $m \geq 2$ can also shift the photocenter slightly because the disk emission is a nonlinear function of the perturbations (see eqs. [42] and [50]) and does not have symmetry after summing up $m \geq 2$ perturbations. The contributions of $m \geq 2$ modes are, however, small.

Figure 7*a* shows the motion of the photocenter of the star-disk system. The disk scattered light significantly affects the motion of the photocenter, which is shown by the solid line. The motion of the disk partly cancels the stellar motion, making the amplitude of the photocenter's motion about two-thirds of that without the disk (*dashed line*). The disk contribution to the motion of the photocenter is significant. In this figure the planet's mass is $1M_J$ ($M_J \approx 10^{-3}\ M_\odot$). For a larger mass planet, however, the disk's relative contribution becomes smaller. Figure 7*b* shows that for a $10M_J$ planet the motion of the photocenter with a disk does not significantly differ from the motion without the disk. The amplitude of the star's dynamical motion is proportional to the planet's mass, while the disk contribution to the motion of the photocenter is not proportional to it. The contrast of the spiral pattern shown in Figure 6 is nearly saturated, even though the planet is as small as Jupiter. Thus, a further increase in the planet's mass causes neither a significant increase in the spiral pattern contrast nor a much larger shift of the photocenter by the disk. A more massive planet results in the decreasing importance of the disk in the photocenter's motion.

4.2.2. *Inclined Disks*

Waves of $m = 2$ and higher do not move the center of mass of a disk and only slightly shift the photocenter of a face-on disk. If a disk is observed at an inclined angle, however, $m \geq 2$ waves also contribute in moving the photocenter. When a flared disk is inclined to the observer, the half on the farther side is illuminated more efficiently than the other half. This imbalance breaks the symmetry of $m \geq 2$ waves.

Figure 8 shows the scattered light image of a disk that is 75° inclined to the line of sight. The bright part of the disk is the

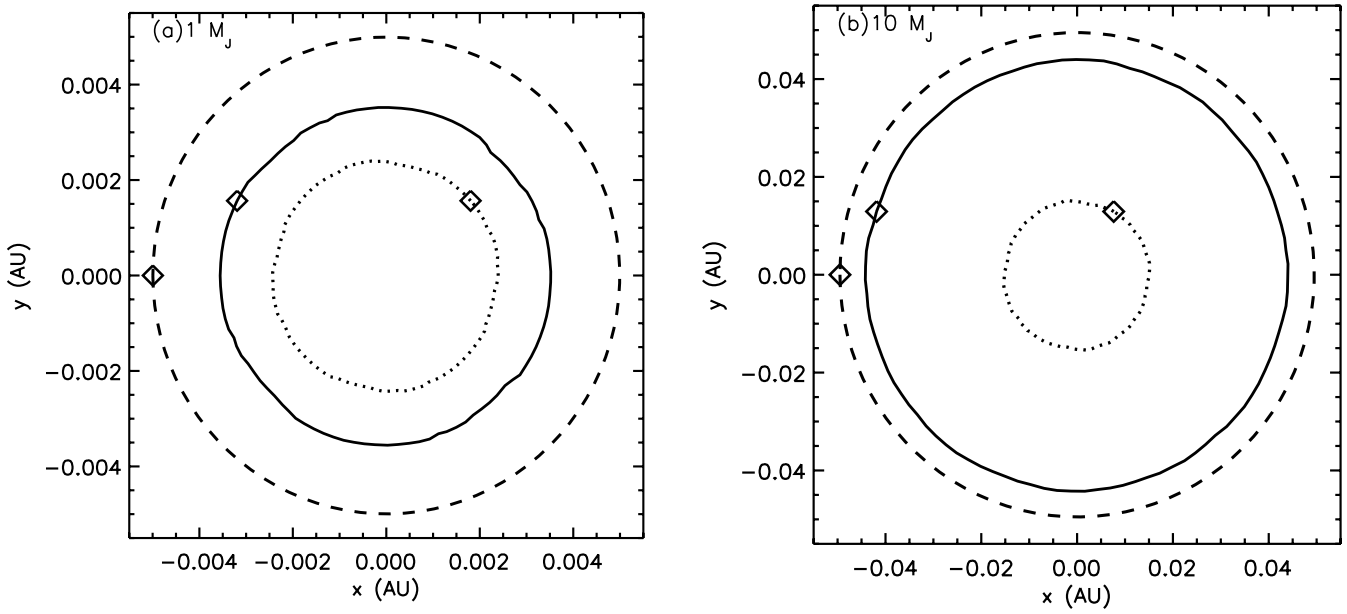

FIG. 7.—Shift of the photocenter for a face-on disk. The solid line shows the motion of the photocenter of the star-disk system. The dashed line shows the motion of the star caused only by the planet, assuming no disk. The dotted line shows the disk's contribution (the difference of the above two results). The diamonds show the positions of the photocenters when the orbital phase of the planet is zero. (*a*) Photocenter motions with a Jupiter mass planet ($M_p = M_J$). (*b*) Motions with a $10M_J$ planet ($M_p = 10M_J$).

side farther from the observer, and the closer side is dark. The position of the photocenter shifts from the star to the bright side. This shift is as large as the disk radius multiplied by the disk-to-star luminosity ratio, $r_d L_d/L$, which is much larger than the amplitude of the stellar wobble. In observations of the stellar position, however, it leads to only an additional offset to the mean stellar position because observational beam sizes are usually larger than the disk radius. An important observational quantity is the motion of the photocenter with time. As the planet orbits, the wave pattern rotates. This causes a fluctuation of the photocenter because only a half-disk is on the bright side. Figure 9*a* shows the motion of the photocenter caused by a $1M_J$ planet. The disk is 60° inclined to the line of sight. We show the relative motions from the average position. The asymmetry of disk light between the bright part and the dark part causes a large offset of the photocenter position from the stellar position, but this offset is subtracted in plotting Figure 9. The presence of the disk changes the orbital shape of the photocenter in addition to enlarging the motion. The amplitude of the disk effect is similar to that in the face-on case. Hence, the disk light interferes with a precise determination of the planet's orbit. For more massive planets, the relative importance of a disk becomes smaller. Figure 9*b* shows that if the planet's mass is as large as $10M_J$, the disk effect is not very significant.

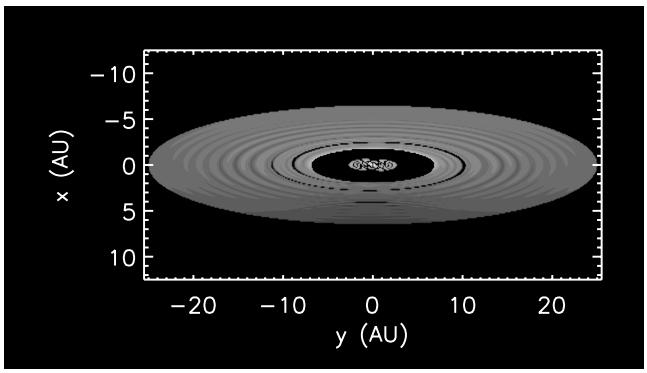

FIG. 8.—Simulated scattered light image of an inclined disk. The disk is perturbed by a Jupiter mass planet ($M_p = M_J$) and viewed at $v = 75°$ ($v = 0$ for a face-on disk). The top half of the disk is the side farther from the observer, while the bottom half is the closer side. Gray scale shows logarithmic values of the disk flux.

4.3. *Various Models*

4.3.1. *Low Viscosity*

In our typical models, we used $\alpha_{\rm vis} = 10^{-2}$ for the viscosity parameter. Here we consider a model with a lower viscosity $\alpha_{\rm vis} = 10^{-3}$. As shown in Figure 2, waves have attenuated before arriving at $r_{\rm out,2} = 5r_p$ for an $\alpha_{\rm vis} = 10^{-2}$ disk. In a low-viscosity disk, however, waves can reach as far as $10r_p$, so we use a disk model with $r_{\rm out,2} = 10r_p$. Figure 10 shows the motion of the photocenter of a 60° inclined disk. The motion of the photocenter has a different orbital shape from that of the high-viscosity disk, although their amplitudes are similar. The wave spiral pattern in a lower viscosity disk extends to a larger region of the disk, leading to a different shift of the photocenter of the disk. This result means that the motion of the disk's photocenter is sensitive to the wave pattern, which changes according to the disk properties. Thus, if the disk contamination of the photocenter is significant, it is difficult to remove this contamination.

4.3.2. *Narrow Gap*

In our typical models, we assume a gap in the range $[0.6r_p, 1.4r_p]$ (where the density is below half the value without the planet). If the planet's mass is larger than $1M_J$, it clears the disk gas from the $m = 2$ inner LR at $0.63r_p$ to the $m = 2$ outer LR at $1.31r_p$ (Lin & Papaloizou 1986; Takeuchi et al. 1996). Thus, the gap size assumed here is the typical value, but we also performed an experiment to see what occurs if the gap is narrower. The motion of the photocenter in Figure 11 is calculated with an assumed gap in the range $[0.8r_p, 1.2r_p]$. The

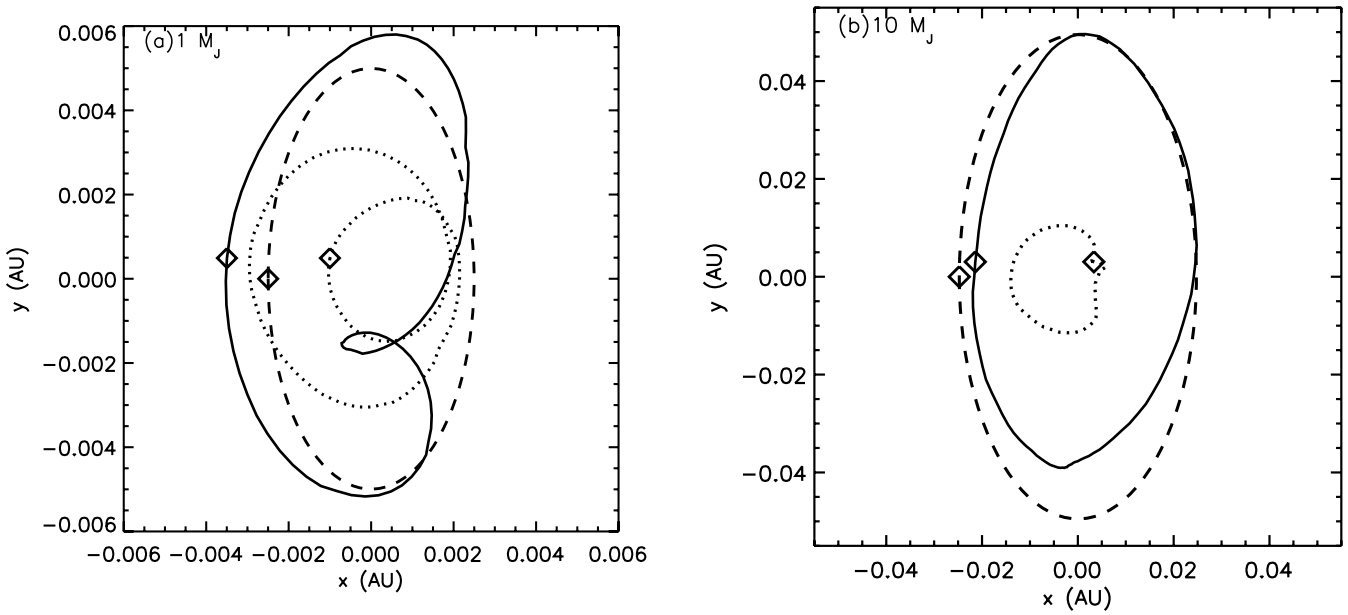

FIG. 9.—Shift of the photocenter. The disk is viewed at an inclined angle $v = 60^\circ$. The solid, dashed, and dotted lines represent shifts in photocenters (see Fig. 7). (*a*) Photocenter motions with a Jupiter mass planet ($M_p = M_J$). (*b*) Motions with a $10M_J$ planet ($M_p = 10M_J$).

narrow gap allows wave excitation of modes as high as $m \approx 6$, while in the wide gap case only $m \lesssim 3$ waves are excited. It causes a stronger disturbance in the disk. The fluctuation of the photocenter induced by the disk is so large that precise measurement of the planet's orbit becomes difficult.

5. ASTROMETRY SHIFT OBSERVED BY *SIM*

The astrometric wobble in the position of a 1 $M_\odot$ star at a distance of 140 pc due to a Jupiter mass planet in a 5 AU orbit is $\sim$36 μas ($\sim$7 μas for 1 AU orbit). The interferometric observations by *SIM* will have the accuracy to measure such small angular displacements. However, *SIM* delay measurements correspond to the position of the photocenter. In order to derive the astrometry parameters of the target star, such as parallax, proper motion, and the star's wobble about the center of mass, we have to assume that the measured photocenter position shifts represent the true astrometry signal of the target. Often it is assumed that the target has only nonluminous stellar or substellar companions. If the target star is not in a clean environment but embedded in a disk, it is likely that the position of the photocenter as measured by *SIM* delay is not a true representation of the target star position.

SIM will have the ability to measure the phase of the complex visibility of the star with unprecedented accuracy. In the visible wavelengths the star is 10^6 times brighter than the planets. Therefore, in the idealized case of a single star with planets, the brightness distribution can be assumed to be point source with the photocenter coincident with the star position.

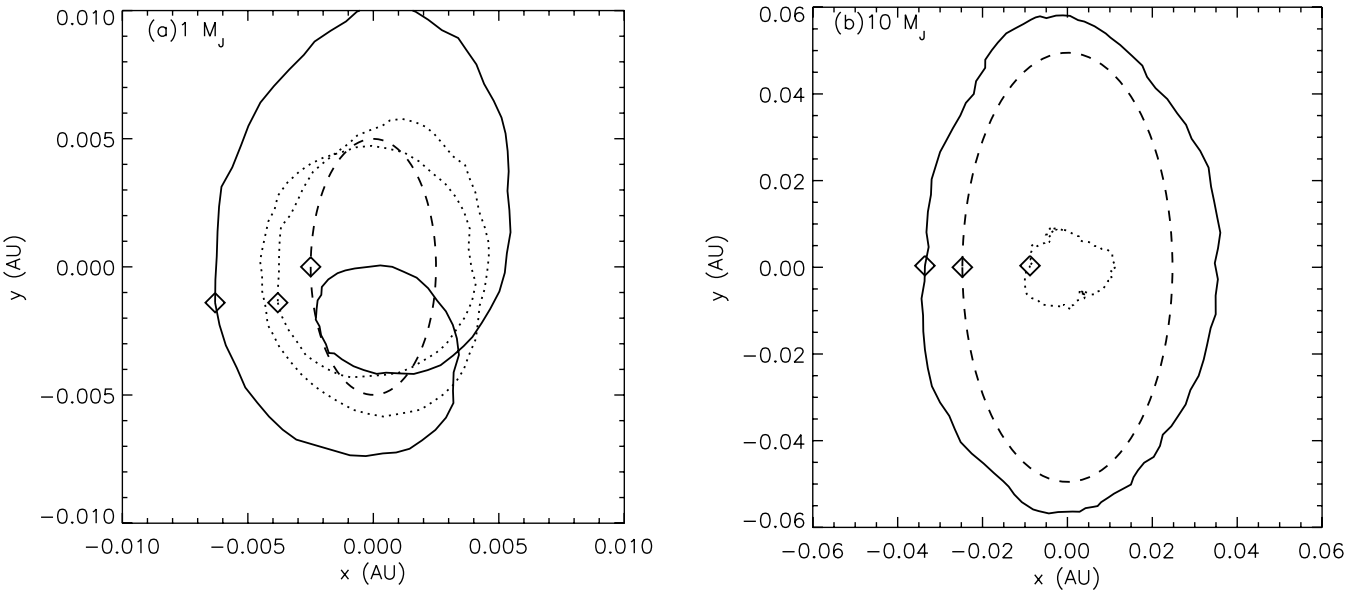

FIG. 10.—Same as Fig. 9 but with a low-viscosity disk $\alpha_{\rm vis} = 10^{-3}$.

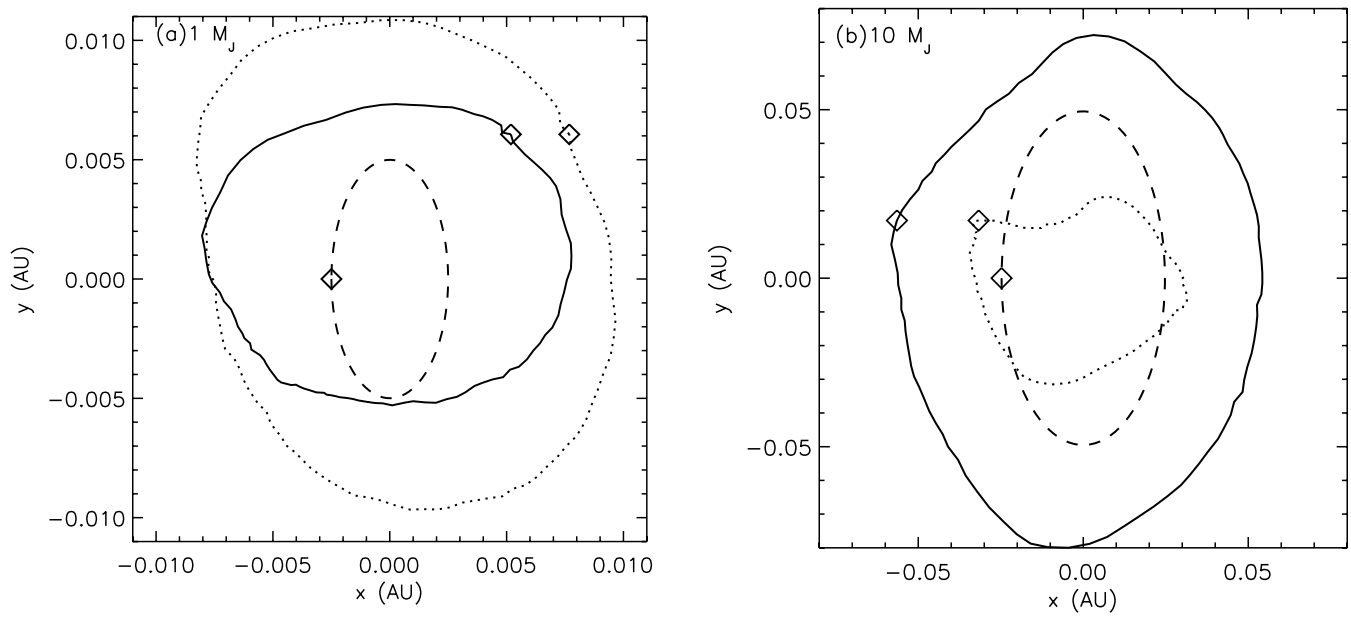

FIG. 11.—Shift of the photocenter with a narrow gap in the range $[0.8r_p, 1.2r_p]$. The disk is viewed at an inclined angle $v = 60^\circ$. The solid, dashed, and dotted lines represent shifts in photocenters (see Fig. 7). (*a*) Photocenter motions with a Jupiter mass planet ($M_p = M_J$). (*b*) Motions with a $10M_J$ planet ($M_p = 10M_J$).

The complex visibility of the brightness distribution has an amplitude unity with the phase changing as the photocenter wobbles around the star-planet center of mass. The visibility phase shift $\Delta\phi$ measured by the interferometer with a baseline $b = 10$ m is related to the angular separation $\Delta\theta$ between the center of mass and the star position:

$$\Delta\phi = \frac{2\pi b}{\lambda}\Delta\theta, \tag{52}$$

where λ is the wavelength. The measured visibility phase $\Delta\phi$ can result from (1) the systemic motion of the target star, (2) the fringe measurement errors due to the photon noise, and (3) the brightness distribution around the target star, such as the scattered light from the disk. The photon and instrumental noises introduce a randomly varying position shift, which can be reduced by longer observing time. However, the photocenter shift induced because of the brightness structures around the star introduces a systematic position error, which varies with time only as the orientation of the baseline changes. This makes interpretation of the measured astrometry signal in terms of wobble induced by planet(s) difficult. It can be partly removed by modeling if we know the target environment well enough.

The disk's contamination of the measured astrometric shift is especially significant if the planet's mass is smaller than about $10M_J$. An interferometer is not too sensitive to structures on a much larger spatial scale than the fringe size λ/b. In the case of an extended source with a uniform brightness, the interferometer fringe visibility decreases with increasing source size $\alpha_{\rm src}$ as $\mathrm{sinc}\,(\pi\alpha_{\rm src}\lambda/b)$, where $\mathrm{sinc}\,x$ is $(\sin x)/x$. It becomes zero when the source size is equal to the fringe size. For *SIM* the fringe size is about 10 mas at 0.5 μm. Although an extended disk with a radially smooth symmetric distribution (with size $\gg$10 mas) will be well within the field of view of *SIM*, its fringes will be washed out significantly and therefore will not contribute to the fringe visibility of the target star. On the other hand, any small-scale structures (size $<$10 mas) present in the scattered light within the *SIM* field of view, such as those caused by disk spirals or gaps, can produce fringes. Thus, the small-scale structures in the disk can contribute to the complex fringe visibility of the target star, resulting in a phase shift that will be interpreted as an astrometry signal.

In this section, we present the results of the simulated astrometry shifts for some of the disk light models. In order to simplify the computations we assumed eight spectral channels covering the wavelength range 400–900 nm. The complex visibility phases of the star-disk structure were computed for each channel for a given orientation of the baseline. We use *SIM* parameters $b = 10$ m and mirror size 33 cm. Using equation (52) we estimate the astrometric position shift for each channel. The final values for astrometry shifts were obtained by averaging over the channels weighted by *SIM* sensitivity in each channel and by the stellar photon flux in each channel. The stellar magnitudes, spectral type, and estimated *SIM* throughput were used to compute the number of photons detected in each spectral channel. For *SIM* throughput we adopted the values obtained from the design team for the aperture, transmission, and detector efficiencies. We also assumed a field stop of 1″, but the bandwidth smearing resulting from combining the astrometry shifts over all channels significantly reduces the effective field of view to 30 mas.

For these simulations we assumed that the objects are at Taurus distance, 140 pc. A Jupiter mass planet orbits at 5 AU from a solar mass star, leading to a motion of the star with an amplitude of 36 μas. The stellar photospheric emission is approximated by a blackbody of 4000 K. The disk scattered light image is constructed on numerical grids of 2001×2001. The star is set on the central grid at (1001, 1001). Figure 12 shows simulated astrometry shifts for *SIM*. We show only the additional shift caused by a disk, by subtracting dynamical shifts induced by a planet. A disk of our typical model is viewed face-on. The amplitude of the measured variation in the photocenter's position is less than 1 μas, which is much smaller than the amplitude of the stellar motion, 36 μas. Figure 13 shows the astrometry shifts for an inclined disk. The disk is

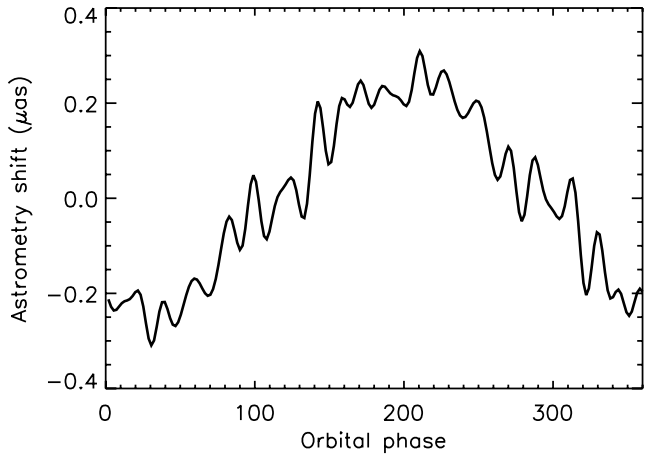

FIG. 12.—Predicted astronomy shift by *SIM* plotted against the orbital phase of the planet. The disk is 140 pc away and observed face-on. A Jupiter mass planet orbits at 5 AU from a solar mass star. The planet's orbital phase is measured from the baseline position angle of *SIM*.

observed at an inclination $v = 60^\circ$. We show the shifts measured with two baselines of *SIM*. One is parallel to the major axis of the disk image, and the other is perpendicular. The amplitudes of the measured variations in the photocenter's position are less than 1 μas. Hence, the presence of a disk does not considerably contaminate the measurement of the stellar position. Figure 14 shows a case in which a planet orbits at 10 AU, which is twice the distance of the typical models. The disk size is doubled to 50 AU. The size of the wave pattern also doubles, and we expect the amplitude of the photocenter's motion to be 2 times larger. The predicted astrometry shifts are, however, comparable to the case of a planet at 5 AU. The scale length of the wave pattern is 2 times larger, and because a larger structure is less sensitive to interferometer observations, the disk has a smaller effect on the astrometry shift. This decrease in the sensitivity nearly cancels out the increase in the photocenter's motion. The dynamical shift by a planet is proportional to the planet's orbital radius. For a planet at 10 AU, the dynamical shift has an amplitude of 71 μas. Hence, the measurement of a planet with a larger orbital radius suffers less contamination by the disk light, although we need a longer observing time to detect such a long-period planet.

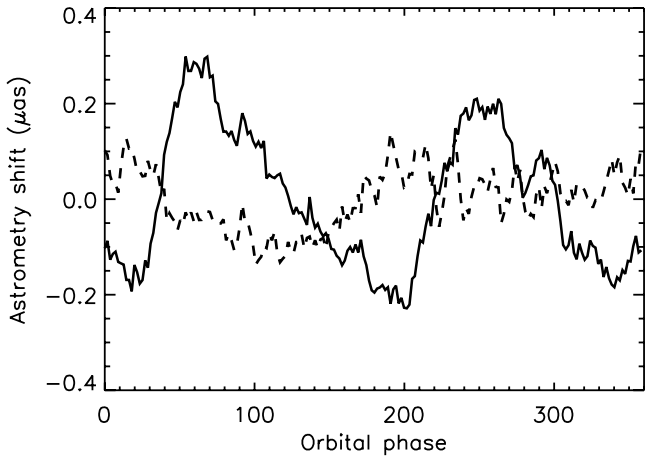

FIG. 13.—Predicted astronomy shift by *SIM* plotted against the orbital phase of the planet. The disk is observed at an inclination $v = 60^\circ$. The solid line shows the shift that is measured with a baseline parallel to the minor axis of the disk image, while the dashed line corresponds to a baseline parallel to the major axis. The planet's orbital phase is measured from the minor axis of the disk image. The disk is 140 pc away, and a Jupiter mass planet orbits at 5 AU from a solar mass star.

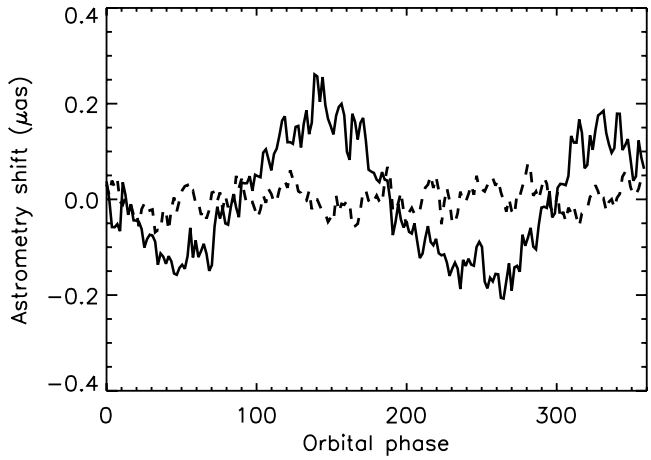

FIG. 14.—Same as Fig. 13, but for a Jupiter mass planet at 10 AU from a solar mass star.

6. CONCLUSIONS

The influence of a circumstellar disk on the motion of the star induced by a planet is analyzed. We show the following:

1. The $m = 1$ disturbance in a disk dynamically moves the stellar position. The disk dynamical effect is, however, much smaller than the planet's gravity and can be neglected.
2. Disk emission moves the photocenter of a star-disk system. In some cases, the disk considerably shifts the photocenter and affects the precise measurement of the stellar position. A significant contamination from the disk occurs if the planet's mass is smaller than $10M_J$ or if the gap in the disk is narrow. For more massive planets, the disk contamination is less important.
3. Actual measurements of the stellar position using an interferometer are insensitive to the extended large-scale structures in the disk surface brightnesses. The *SIM* measurement, for example, does not suffer significant contamination from the scattered light of the disk.

We consider the above results to provide an upper limit of the disk light contamination because our models assume maximum contrast of the disk spiral pattern (see § 4). In addition, the dust residing above the disk scatters the starlight and illuminates the disk surface with a large incident angle. This secondary illumination from the upper dust also reduces the disk's contrast. Hence, in actual disks, the disk light contamination is probably smaller. We need a more realistic radiative transfer calculation in order to take account of such effects and to evaluate precise values of the disk light contamination.

In this paper, the planet's orbit is assumed to be circular. A planet in an eccentric orbit opens a wider gap than a planet in a circular orbit (Artymowicz & Lubow 1994). Because a wider gap suppresses the wave excitation, the disk's spiral pattern is weaker. Hence, for a planet in an eccentric orbit, the disk's contamination is less important. If the planet's orbit is inclined to the disk, however, the planet excites bending waves (Shu et al. 1983; Artymowicz 1994; Ostriker 1994), which may have a large amplitude of wavy pattern on the disk surface. In such cases, the disk's contamination may be more significant than that estimated in this paper and should be examined in future work.

We thank L. Hartmann, C. Beichman, and G. Bryden for useful conversations and P. S. Lykawka for comments. We also thank the referee for useful comments. This work was supported in part by NSF grant AST 99-87417 and in part by a special NASA astrophysical theory program that supports a joint Center for Star Formation Studies at UC Berkeley, NASA-Ames Research Center, and UC Santa Cruz. This work was also supported by NASA NAG5-10612 through its Origin program and by JPL 1228184 through its *SIM* program and by the 21st Century COE Program of Japan, Origin and Evolution of Planetary Systems.

APPENDIX A

DERIVATION OF THE DISK THICKNESS FROM THE TWO-DIMENSIONAL DENSITY AND PRESSURE

In this appendix, we derive the disk half-thickness from the two-dimensional values of the density and the pressure (eq. [34]). Integrating the gas density ρ (eq. [32]) in the z-direction gives the surface density,

$$\sigma = 2\int_0^\infty \rho\, dz = \rho_{\rm mid} h B\left(\frac{1}{2}, \frac{1}{\gamma_3 - 1} + 1\right). \tag{A1}$$

The beta function B is

$$B\left(\frac{1}{2}, a + 1\right) = \frac{\Gamma(1/2)\Gamma(a+1)}{\Gamma(a + 3/2)} = 2\int_0^1 (1 - x^2)^a\, dx, \tag{A2}$$

where Γ is the gamma function. The two-dimensional pressure is similarly

$$P = 2\int_0^\infty p\, dz = p_{\rm mid} h B\left(\frac{1}{2}, \frac{\gamma_3}{\gamma_3 - 1} + 1\right). \tag{A3}$$

Using equations (A1) and (A3) with the relation

$$B\left(\frac{1}{2}, \frac{\gamma_3}{\gamma_3 - 1} + 1\right) = \frac{2\gamma_3}{3\gamma_3 - 1} B\left(\frac{1}{2}, \frac{1}{\gamma_3 - 1} + 1\right), \tag{A4}$$

the disk half-thickness (eq. [33]) is

$$h = \frac{1}{\Omega}\sqrt{\frac{2\gamma_3}{\gamma_3 - 1}\frac{p_{\rm mid}}{\rho_{\rm mid}}} = \frac{1}{\Omega}\sqrt{\frac{3\gamma_3 - 1}{\gamma_3 - 1}\frac{P}{\sigma}}. \tag{A5}$$

From equations (A1), (A3), and $h \propto \rho_{\rm mid}^{(\gamma_3 - 1)/2}$, we see the relation between the two- and three-dimensional γ's as $\gamma = (3\gamma_3 - 1)/(\gamma_3 + 1)$. Then, the disk half-thickness is

$$h = \frac{1}{\Omega}\sqrt{\frac{2\gamma}{\gamma - 1}\frac{P}{\sigma}}, \tag{A6}$$

which is identical to equation (34).

APPENDIX B

LOCATION OF THE PHOTOSURFACE

In § 4.1, it is assumed that the starlight scatters at the disk surface (r, θ, h) at which the gas density drops to zero. The realistic scattering, however, occurs at the photosurface of constant optical depth, which is below the disk surface. In this Appendix, we examine this assumption. The optical depth at (r, θ, h) to the starlight is

$$\begin{aligned}\tau &\sim \frac{1}{\cos\alpha}(h - z)\rho(z)\kappa \\ &\sim \frac{1}{\cos\alpha} 2^{1/(\gamma_3 - 1)}\, \kappa\rho_{\rm mid} h\left(\frac{h - z}{h}\right)^{\gamma_3/(\gamma_3 - 1)},\end{aligned} \tag{B1}$$

where α is the incident angle of the starlight and κ is the opacity, which is $\sim$100 for the visible light if the dust-to-gas ratio is similar to the solar abundance and the dust is well mixed with the gas (Miyake & Nakagawa 1993). In the second equality, equation (32) is used. The condition of the photosurface, $\tau = 1$, reduces to

$$\frac{h - z}{h} \sim 2^{-1/\gamma_3}\left(\frac{\cos\alpha}{\kappa\rho_{\rm mid} h}\right)^{(\gamma_3 - 1)/\gamma_3}. \tag{B2}$$

We use the values at 10 AU: $\gamma_3 = 1.4$, $\cos\alpha \approx (dh/dr - h/r) \sim 0.1$, $\kappa \sim 100$ cm^2 g^{-1}, $\rho_{\rm mid} \sim 10^{-11}$ g cm^{-3}, and $h \sim 10^{13}$ cm. Equation (B2) becomes $(h - z)/h \sim 0.02$. Thus, the photosurface almost coincides with the disk surface. However, we are considering an era after the formation of gas giant planets. If most of the dust has become large bodies, the opacity κ is greatly reduced. In addition, the dust sedimentation to the midplane also reduces the opacity near the disk surface. These effects may shift the photosurface significantly below the disk surface and are the subject of future investigations.

REFERENCES

Artymowicz, P. 1994, ApJ, 423, 581
Artymowicz, P., & Lubow, S. H. 1994, ApJ, 421, 651
Bate, M. R., Lubow, S. H., Ogilvie, G. I., & Miller, K. A. 2003, MNRAS, 341, 213
Benedict, G. F., et al. 2002, ApJ, 581, L115
Bennett, D. P., et al. 1999, Nature, 402, 57
Boss, A. P. 1997, Science, 276, 1836
———. 1998, Nature, 393, 141
Burrows, A., et al. 1997, ApJ, 491, 856
Charbonneau, D., Brown, T. M., Latham, D. W., & Mayor, M. 2000, ApJ, 529, L45
D'Angelo, G., Henning, T., & Kley, W. 2003, ApJ, 599, 548
Danner, R., & Unwin, S. 1999, *SIM*: Taking the Measure of the Universe (Pasadena: JPL)
Goldreich, P., & Tremaine, S. 1979, ApJ, 233, 857
Hayashi, C., Nakazawa, K., & Nakagawa, Y. 1985, in Protostars and Planets II, ed. D. C. Black & M. S. Matthews (Tucson: Univ. Arizona Press), 1100
Ida, S., & Lin, D. N. C. 2004, ApJ, 604, 388
Ikoma, M., Nakazawa, K., & Emori, H. 2000, ApJ, 537, 1013
Kenyon, S. J., & Hartmann, L. 1995, ApJS, 101, 117
Kokubo, E., & Ida, S. 1998, Icarus, 131, 171
———. 2000, Icarus, 143, 15
Konacki, M., Torres, G., Jha, S., & Sasselov, D. D. 2003a, Nature, 421, 507
Konacki, M., Torres, G., Sasselov, D. D., & Jha, S. 2003b, ApJ, 597, 1076
Korycansky, D. G., & Pollack, J. B. 1993, Icarus, 102, 150
Lin, D. N. C., & Papaloizou, J. C. B. 1986, ApJ, 307, 395
Lissauer, J. J. 1993, ARA&A, 31, 129
Lubow, S. H., Seibert, M., & Artymowicz, P. 1999, ApJ, 526, 1001
Marcy, G. W., & Butler, R. P. 1998, ARA&A, 36, 57
Mayor, M., & Queloz, D. 1995, Nature, 378, 355
McGrath, M. A., et al. 2002, ApJ, 564, L27
Miyake, K., & Nakagawa, Y. 1993, Icarus, 106, 20
Monnier, J. D. 2003, Rep. Prog. Phys., 66, 789
Nagasawa, M., Lin, D. N. C., & Ida, S. 2003, ApJ, 586, 1374
Ostriker, E. C. 1994, ApJ, 424, 292
Perryman, M. A. C. 2000, Rep. Prog. Phys., 63, 1209
Podolak, M. 2003, Icarus, 165, 428
Pollack, J. B., Hubickyj, O., Bodenheimer, P., Lissauer, J. J., Podolak, M., & Greenzweig, Y. 1996, Icarus, 124, 62
Rice, W. K. M., Armitage, P. J., Bate, M. R., & Bonnell, I. A. 2003, MNRAS, 338, 227
Schneider, J. 2004, The Extrasolar Planets Encyclopaedia (Paris: CNRS), http://www.obspm.fr/encycl/encycl.html
Shu, F. H., Cuzzi, J. N., & Lissauer, J. J. 1983, Icarus, 53, 185
Sozzetti, A., Casertano, S., Brown, R. A., & Lattanzi, M. G. 2002, PASP, 114, 1173
Takeuchi, T., Miyama, S. M., & Lin, D. N. C. 1996, ApJ, 460, 832
Tanigawa, T., & Watanabe, S. 2002, ApJ, 580, 506
Thommes, E. W., Duncan, M. J., & Levison, H. F. 2003, Icarus, 161, 431
Ward, W. R. 1986, Icarus, 67, 164